energies

Article

Microscopic Study of Shale Anisotropy with SEM In Situ Compression and Three-Point Bending Experiments

Weibo Sui [1,*], Yulong Wang [2] and Junwei Li [1]

1 College of Petroleum Engineering, China University of Petroleum (Beijing), Beijing 102249, China
2 Petroleum Engineering Research Institute of Dagang Oilfield Company, Tianjin 300280, China
* Correspondence: suiweibo@cup.edu.cn

Abstract: The microscopic anisotropy of shale has an important impact on its mechanical properties and crack behavior, so it is essential to understand the microscopic origin of anisotropic growth with a more effective laboratory work scheme. Uniaxial compression test and three-point bending test are considered to be efficient means to study the elastic properties and crack behavior of rocks. In this paper, uniaxial compression experiments and three-point bending experiments were conducted on shale outcrops in the Changqing area using field emission scanning electron microscopy (SEM) and in situ tensile testing, and the microscopic deformation and crack processes were quantitatively characterized by the digital image correlation (DIC) method. For the compression experiments, the observation of the first principal strain fields indicated that the microscopic anisotropy of shale was related to the bedding planes, and the microscopic deformations were mainly concentrated in the clay mineral accumulation area and at the microcracks. Elastic moduli and compressive strengths of specimens with different bedding angles were affected by the strong shear stress effects. The specimens with a bedding angle of 30° showed lower peak loads and compressive strengths, and the specimens with a bedding angle of 60° had lower elastic moduli. Three-point bending experiments were conducted for studying the effects of crack-bedding orientation relationships on cracking processes, and four critical fracturing mechanical properties were calculated. The short transverse-type cases were prone to break and had a lower peak load, tensile strength, fracture toughness and elastic-bending modulus. The divider-type cases were more difficult to break, formed a more tortuous crack and had a higher tensile strength, fracture toughness and elastic-bending modulus. The arrester-type cases had a middle range of mechanical parameters but developed the longest cracks. This study provides a feasible experimental and analysis method for understanding the microscopic anisotropy of shale samples. The small specimen size also makes the requirements of core samples easier to be satisfied considering the field application. Furthermore, the anisotropy of cracking processes can be understood better by building the connections between microstructural characteristics and mechanical performances.

Keywords: microscopic anisotropy; scanning electron microscopy (SEM); digital image correlation (DIC); in situ compression experiment; three-point bending experiment

check for updates

Citation: Sui, W.; Wang, Y.; Li, J. Microscopic Study of Shale Anisotropy with SEM In Situ Compression and Three-Point Bending Experiments. *Energies* **2023**, *16*, 2440. https://doi.org/10.3390/en16052440

Academic Editors: Dameng Liu and José António Correia

Received: 25 December 2022
Revised: 11 February 2023
Accepted: 24 February 2023
Published: 3 March 2023

1. Introduction

Shale gas and oil resources have become the focus of Chinese oil and gas exploration and development and will be vigorously developed in the future. Shale has pre-existing bedding structures and naturally formed microfractures, which make its mechanical properties and deformation characteristics quite different from those of conventional oil and gas reservoir rocks [1,2].

Many scholars have found that shale develops a typical bedding structure during the process of sediment consolidation and diagenesis. The macroscopic anisotropy of shale has been studied for its elastic properties and fracturing mechanism. Through macroscopic uniaxial/triaxial compression experiments and Brazilian splitting experiments on shale samples at different sampling angles, researchers have proven that the elastic modulus, shear modulus and Poisson's ratio of shale vary with the bedding angle [3–5]. In addition, Lo et al. [6] used Chicopee shale samples to analyze the anisotropy of shale under different confining pressures and proved that when the confining pressure was high, shale rock samples still had anisotropic characteristics, and these characteristics were caused by the internal microstructural features of shale.

In addition, through experimental studies and theoretical simulations of shale macroscopic cracking processes, it was determined that the high compressibility and weak cementation of shale bedding can lead to anisotropic characteristics in the deformation law, permeability evolution, compressive strength, fracture toughness and crack evolution law of shale rock [7,8]. Chandler et al. [9] reported fracture toughness measurements on Mancos shale determined in all three principal fracture orientations, namely, divider, short transverse and arrester, using a modified short-rod methodology. Significant anisotropy was observed in shale fracture toughness measurements under ambient conditions. Chong et al. [10] used PFC (Particle Flow Code) software to simulate the failure process of shale samples with bedding structure characteristics using the Brazilian splitting experiment and analyzed the influence of parameters such as the dip angle and strength of shale bedding on the failure law. The particle flow code (PFC) is a type of Discrete Element Method, which is commercially available and now widely used to solve many rock engineering and geomechanics problems [11].

The digital image correlation (DIC) method is one of the optical measurement methods for quantifying the deformation and cracking behaviors of rock specimens at the microscale. Its basic principle is to track geometric points in a random digital speckle image on the specimen surface before and after deformation to determine the displacement field of the specimen [12]. For example, Wang et al. [13] applied the DIC method in analyzing the swelling of mudstone specimens under different humidity conditions and further applied it to shale specimens [14]. Under different humidity conditions, the heterogeneous strain field captured by the DIC analysis indicated the swelling of clay minerals was hindered by the non-swelling inclusions and local stresses were generated. The transition of deformation modes with increasing humidity was also investigated by using the strain maps provided by DIC analysis. Zhou et al. [15] studied the crack initiation and propagation of shale central straight-notched Brazilian disks (CSNBD) under different loading angles by the DIC method. Li et al. [16] conducted three-point bending fracture experiments on a semicircular shale with different bedding angles combined with DIC to study the influence of bedding on crack evolution. The DIC strain field analysis clearly showed three stages during three-point bending: uniform strain distribution, damage accumulation, and strain localization. It also should be mentioned that considerable tensile strain localization extending from the tip of the prefabricated crack was characterized by DIC analysis in each specimen.

To explore the relationship between shale microstructure, mineral composition and macroscopic anisotropy, Gao et al. [17] used SEM and energy dispersive spectroscopy (EDX) to analyze the microstructure and composition characteristics of shale and showed the tensile-compression properties of shale and the variation in shale acoustic characteristics with bedding angle under an external force. Using experimental methods such as focused ion beam cutting (FIB) and atomic force microscopy (AFM), parameters such as Young's modulus of shale surface microregions can also be measured, and the corresponding relationship between mineral composition and modulus can be studied [18,19]. Wu et al. [20] presented a cross-scale and statistical nanoindentation technique to measure Young's modulus at different length scales for three differently oriented samples. The elastic moduli of individual minerals at the microscale and the bulk rock at the macroscale were both determined. The study also proved that the shale possesses multiscale elastic anisotropy.

Generally, experimental research methods regarding the anisotropy of shale mechanical properties and fracture modes have mainly been concentrated on the macroscopic scale, with relatively few corresponding micro-experimental methods. In this paper, in situ compression experiments and three-point bending experiments were carried out on shale outcrop samples in the Changqing area using SEM with an in situ tensile stage. The displacement and strain fields of the specimen surface were quantitatively characterized by the DIC method. Combined with the initiation, propagation and extension of cracks to fracture, the anisotropic characteristics of mechanical properties and fracture processes at the mesoscopic scale of shale samples were analyzed.

2. Experimental Methods

2.1. Sample Preparation

The tested shale was taken from outcrops of the Changqing area, Ordos Basin, which is one of the major shale gas productive regions in China. The results of Rietveld refinement (Table 1) indicate that the main mineral constituents of shale samples are quartz and carbonates cemented by clay, which account for 37.5% and 35.7% of the total, respectively. The main component of clay is illite. The QFP (quartz, feldspar, pyrite) and carbonates are considered brittle minerals; thus, the tested shale is brittle, and its porosity and permeability are 1.91% and 0.0031 mD, respectively.

Table 1. Rietveld refinement results of the shale samples.

Mineral Types	Quartz	Dolomite	Calcite	Potassium Feldspar	Plagioclase	Pyrite	Clay
Mass percentage (%)	37.5	21.3	14.4	0.4	5.0	2.3	18.9

For the SEM uniaxial compression experiment, cuboid specimens with dimensions of 8 mm × 6 mm × 6 mm were selected in this study (Figure 1a). The surface of the specimen was polished with fine sand and then an argon ion beam. The polished surface was coated with a thin layer of carbon, which is suitable for SEM imaging. Taking different directions of the bedding plane into consideration, the angles θ between the loading direction and the bedding plane were set to 0°, 30°, 60° and 90° for the four testing groups, as shown in Figure 1b. Six specimens were prepared for each group of uniaxial compression experiments. The specimen was named $A°$-B. For example, 60°-2 denotes specimen No. 2 with θ = 60°.

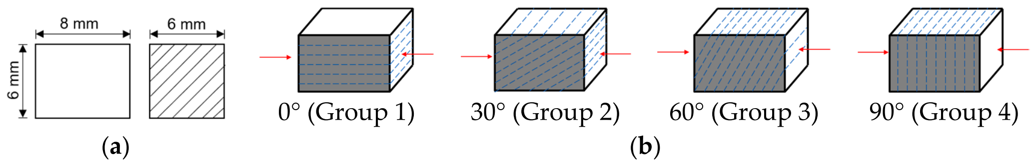

Figure 1. Preparation of the shale cuboid specimens for the in situ uniaxial compression experiments: (**a**) Schematic diagram of the specimen and (**b**) 4 testing groups with different angles between loading direction and bedding plane.

For the SEM three-point bending experiment, beam specimens with dimensions of 50 mm × 5 mm × 8 mm were selected (Figure 2a). Following the definitions given by Schmidt [21] and Chong et al. [22], three types of specimens for the three-point bending experiment were prepared, including arrester (A), divider (D) and short-transverse (ST). The definition is based on the crack orientation relative to the bedding plane, as shown in Figure 2b. The surface of the specimen was also treated as above. Meanwhile, a thin saw blade was used to prefabricate a straight notch (i.e., Mode I precrack) with a length of 0.6 mm and a width of 0.4 mm at the center of the bottom of the specimen. Six specimens were prepared for each group of three-point bending experiments. The specimen was named A-B. For example, ST-2 denotes specimen No. 2 with a short transverse orientation.

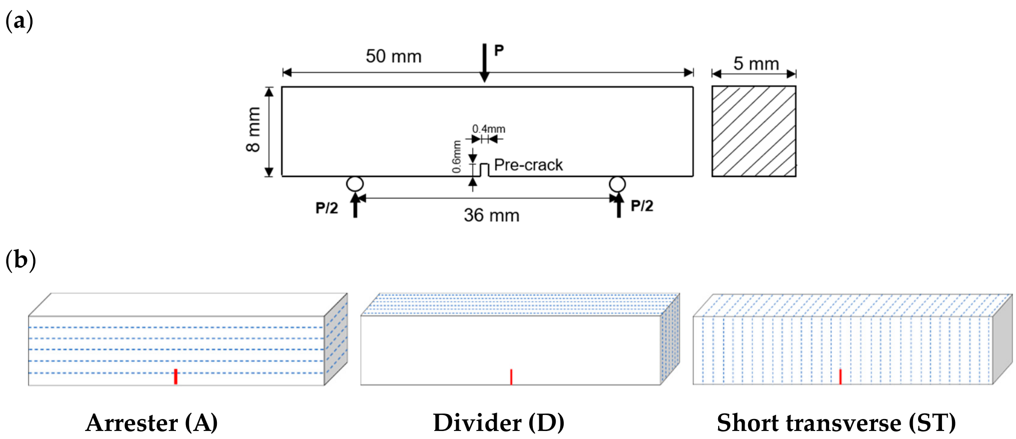

Figure 2. Preparation of the shale beam specimens for the three-point bending experiments: (**a**) Schematic diagram of the three-point bending specimens and (**b**) the three crack orientations relative to the bedding planes.

2.2. Experimental Procedures

The experiments were conducted using a Zeiss Sigma 500 FE-SEM with an in situ tensile stage Gatan Microtest 5000 (facilities of China University of Petroleum (Beijing), China). Uniaxial compression tests and three-point bending tests were performed in the FE-SEM chamber by using a compression clamp and three-point bending clamp, respectively (see Figure 3). To hold the specimen at the proper position in the compression or three-point bending clamp, a preload of 10 N was applied before the test. The experimental results showed no deformation effects were caused by this preload. Both the compression and three-point bending experiments were conducted in displacement-controlled mode at a rate of 1.67 μm/s, and the images were obtained in backscattered electron mode at a voltage of 20 kV. The loading rate is one of the crucial parameter which affects the strength and deformation response of bounded materials such as rocks and cemented soil. More information about determining the reasonable loading rate can be found in some studies listed here [23–26].

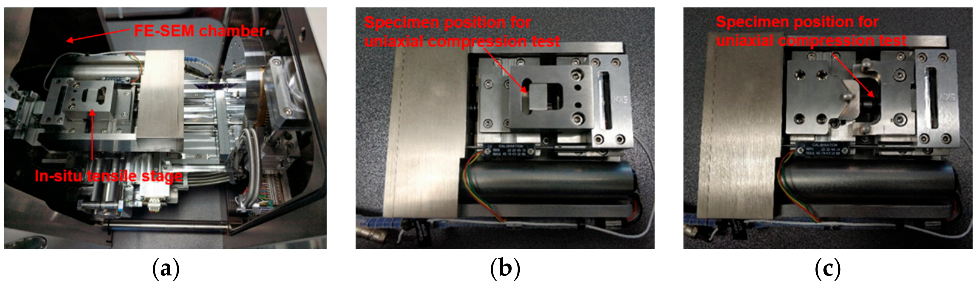

Figure 3. Experimental equipment: (**a**) In situ tensile stage loaded in the SEM chamber; (**b**) Specimen position in the compression clamp; (**c**) Specimen position in the three-point bending clamp.

In each testing group, six specimens were used. For the compression experiments, three specimens were pretested outside of the chamber for the peak load, and the formal compression tests for the other three specimens were conducted in the chamber to reach 85% of the peak load. For three-point experiments, the pretests for peak load were carried out in the same way, and the formal tests were conducted up to the failure of the specimens. The pretesting results are listed in Table 2. From the pretesting of the shale specimens prepared for the compression test, we can find that the 0° shale specimens have the maximum peak load due to their critical compaction process. In addition, the standard deviation of results increases with the increase in angles θ between the loading direction and the bedding plane, which may be caused by the lateral deformation effects. With the increase in angles θ between the loading direction and the bedding plane, the bedding planes lead to nonuniform lateral deformation effects as mechanically weak surfaces, and caused more severe failure randomness during compression tests.

Table 2. The pretesting results for the compression test and three-point bending test.

Group	Specimen	Length (mm)	Width (mm)	Thickness (mm)	Peak Load (N)	Average Peak Load (N)	Standard Deviation of the Peak Load (N)
0°	0°-1	8.10	6.10	5.90	2199.67	2234.43	28.37
	0°-2	8.10	6.05	5.84	2234.48		
	0°-3	8.00	6.08	5.90	2269.15		
30°	30°-1	8.04	5.90	5.92	1200.51	1322.79	107.70
	30°-2	8.10	5.90	5.90	1462.58		
	30°-3	8.06	5.94	5.92	1305.29		
60°	60°-1	8.10	5.90	5.92	2221.18	2048.30	128.45
	60°-2	8.08	5.94	5.94	1913.57		
	60°-3	8.06	5.90	5.94	2010.15		
90°	90°-1	7.90	5.90	5.90	2399.83	2199.76	311.00
	90°-2	7.95	6.00	5.88	1760.52		
	90°-3	8.08	5.90	5.84	2438.93		
Arrester (A)	A-1	50.04	5.06	8.02	210.4	202.23	6.11
	A-2	50.02	5.00	8.08	200.6		
	A-3	50.10	5.04	8.06	195.7		
Divider (D)	D-1	50.04	5.06	8.02	165.7	170.57	4.69
	D-2	50.02	5.00	8.08	169.1		
	D-3	50.10	5.04	8.06	176.9		
Short Transverse (ST)	ST-1	50.06	5.04	8.06	48.5	47.53	0.92
	ST-2	50.08	5.04	8.06	46.3		
	ST-3	50.12	5.02	8.04	47.8		

By using a series of SEM images captured during the loading process, the DIC technique can be applied to accurately analyze the microscopic deformation behavior and cracking procedure. The basic concept of DIC is to compare two images of a component before and after deformation. Displacements and strains are determined by correlating the position of pixel subsets or blocks in the original and deformed image, normally based upon contrast (i.e., gray intensity levels). In this study, the DIC in-house software VIDI was used for the two-dimensional DIC calculations.

3. Experimental Results

3.1. Microscopic Deformation Characteristics during Compressive Loading

Compared with other types of rocks, the microscopic pore structure of shale is more complex, and the pore diameter in shale varies widely, including micron-scale fractures and several nanosized pores. These pores and fractures together form fluid flow channels in the shale. According to the classification method given by Loucks et al. [27], shale matrix pores include intergranular pores, intragranular pores and organic matter pores. The different shapes, sizes and types of pores in shale lead to the complexity and heterogeneity of the microscopic pore structure of shale, which will affect the deformation of the microstructure of shale under loading. Here, we show the microscopic deformation characteristics of shale during uniaxial compression tests due to the influence of bedding planes and clay minerals.

Figures 4–6 show the strain field and strain concentration of the surface of shale specimens for various bedding plane inclination angles. The microscopic deformations of the shale specimens were closely related to the expansion and compression of the microcracks and the shear dislocation of clay minerals.

Figure 4a depicts the first principal strain (E_1) cloud chart of the shale specimen under a compression load of 1234.8 N and θ = 0°. The size of the microcracks on the surface of the specimen was between tens of nanometers and several micrometers, and most of the microcracks were parallel to the bedding planes (Figure 4b). The high strain area was mainly concentrated near the microcracks and is shown in red, and the horizontal banded distribution indicates that the microcracks expanded in the direction perpendicular to the bedding planes.

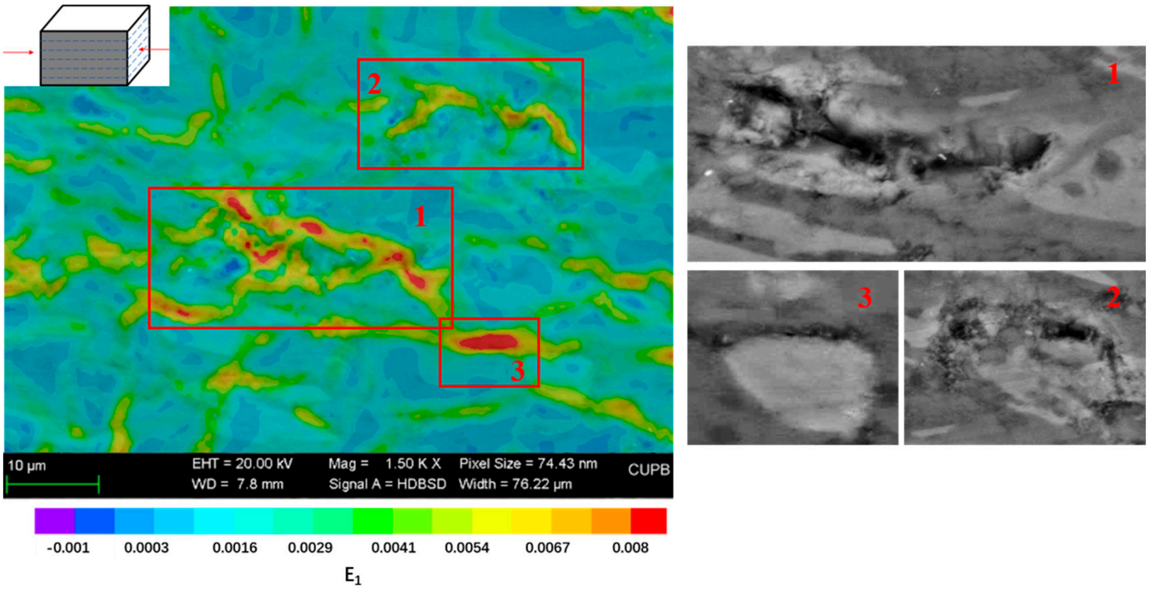

(**a**) (**b**)

Figure 4. Microstructure deformation when bedding angle is 0°: (**a**) E_1 cloud chart; (**b**) 3 microcracks. The marked numbers correspond to the positions in Figure 4a.

Figure 5 depicts the horizontal strain (E_{xx}) cloud chart of the shale specimen when $\theta = 60°$ and the load of 828 N. The results indicate that the microcracks of the specimen were generally consistent with the bedding trend. In addition, the high strain of the specimen mainly occurred near the crack and was blue when the specimen was under stress, which indicates that the microfractures showed a closing trend.

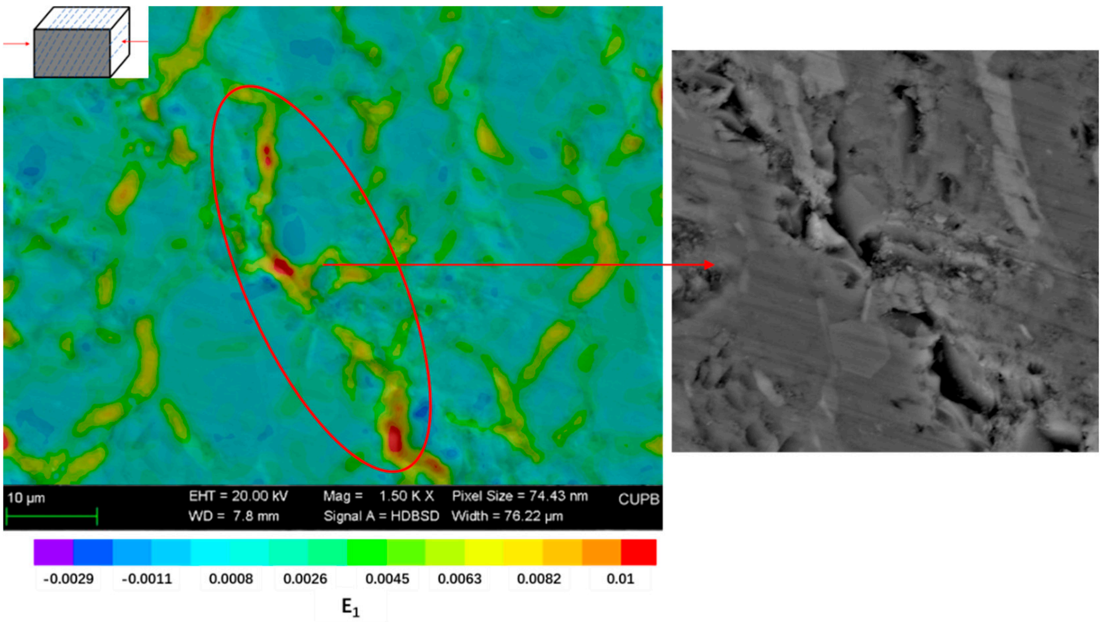

(**a**) (**b**)

Figure 5. Microstructure deformation when the bedding angle is 60°: (**a**) E_1 cloud chart; (**b**) Zoomed-in microcracks in the circled region.

Figure 6 shows the first principal strain (E_1) cloud chart for θ = 90°, and the compression load was 1220.4 N. These data show that the microscopic deformation of shale specimens in the clay mineral accumulation area was very complex. As shown in the E_1 cloud chart of Figure 6a, in the clay mineral accumulation area within the red box, there was both a clay mineral expansion area (red) and a compressed area (blue). The reason is that due to the disordered arrangement of clay minerals, the shear strain was generated by the different degrees of internal deformation of the specimen after being subjected to compressive loads, resulting in the concentration of positive and negative strains in the clay minerals simultaneously.

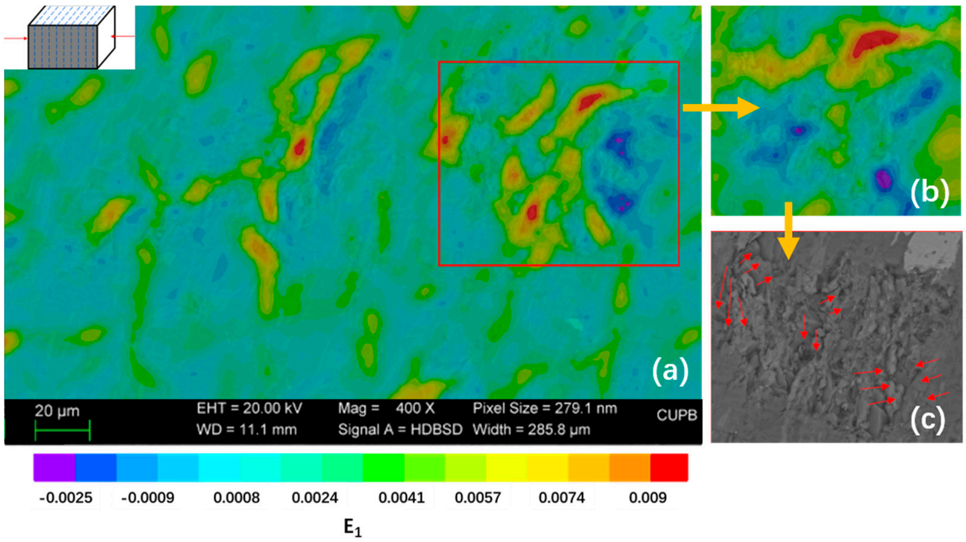

Figure 6. Microstructure deformation when the bedding angle is 90°: (**a**) E_1 cloud chart; (**b**) E_{xy} cloud chart of the framed region in Figure 6a; (**c**) Clay minerals of the framed region in Figure 6a, and the arrows indicate expansion or compression of clay minerals.

3.2. Microscopic Cracking Process and Crack Path in Three-Point Bending Tests

The microscopic crack initiation and propagation of shale specimens with three different crack-bedding relationships were studied by conducting three-point bending tests. Figures 7–9 show the load–displacement curves obtained from the three-point bending tests on shale specimens with different crack types. All of the load–displacement curves exhibited approximately linear growth and a sudden drop after passing the peak load points. Meanwhile, different groups of crack types showed some distinct features.

The load–displacement curves revealed that the peak load of the type-A specimen was the maximum, then type-D, and the type-ST was the minimum, much lower than the other two types (Table 2). This result indicates that the type-A specimen has the strongest resistance to fracture, and vice versa for the type-ST specimen.

Combined with the DIC strain field analysis, we can see how the crack-bedding orientation relationship affected the crack initiation and propagation. For type-ST and type-A crack cases, the crack initiation point can be located clearly from the strain field changes. Before crack initiation, the strain field did not show any strain concentration around the notch tip area (Figures 7b and 8b). At a certain loading stage, a clear strain concentration appeared and indicated crack initiation (Figures 7c and 8c), and the SEM images also showed microcrack formation (Figures 7e and 8e). When the load continued to increase to the failure point, the microcracks propagated to form a main crack, and the peak load suddenly dropped (Figures 7d and 8d). Compared with the type-A crack case, the type-ST crack showed much earlier crack initiation, which is supported by the fracture toughness calculation given in the later part.

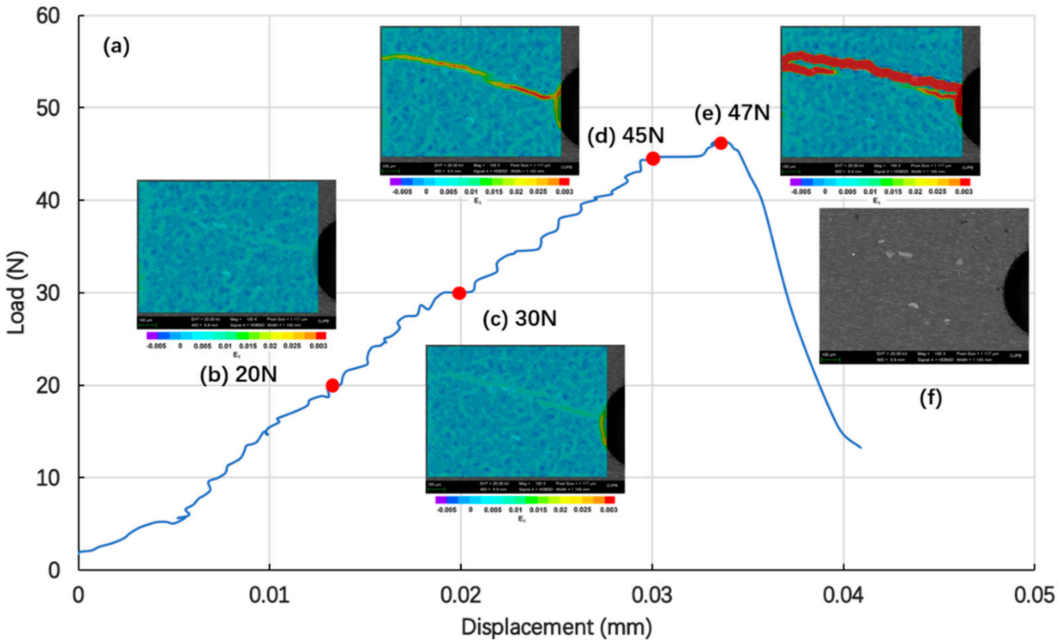

Figure 7. Cracking process in group ST−2: (**a**) load–displacement curve for group ST−2; (**b**) E_1 cloud chart at a load of 20 N; (**c**) E_1 cloud chart at a load of 30 N; (**d**) E_1 cloud chart at a load of 44 N; (**e**) E_1 cloud chart at a load of 47 N and (**f**) zoomed out SEM image of the crack.

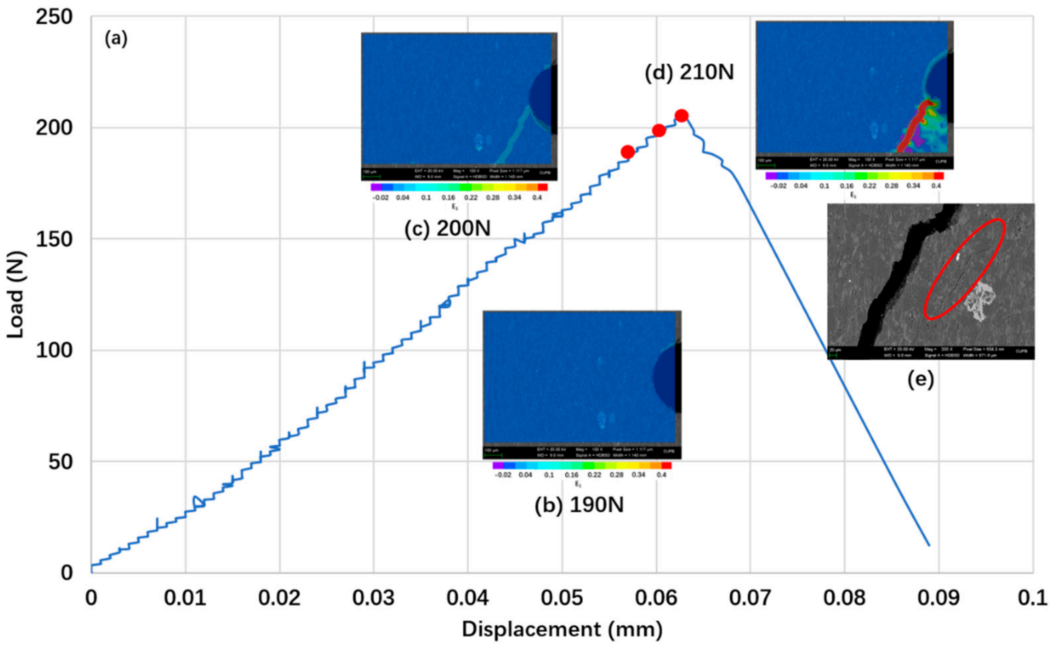

Figure 8. Cracking process in Group A−1: (**a**) load–displacement curve for Group A−1; (**b**) E_1 cloud chart at a load of 190 N; (**c**) E_1 cloud chart at a load of 200 N; (**d**) E_1 cloud chart at a load of 210 N and (**e**) zoomed out SEM image of the crack.

However, the type-D crack case did not show a clear crack initiation point, and a sudden failure was observed based on the strain field analysis (Figure 9), which can be explained by the following fracture property analysis. The magnified SEM images of cracks show that the type-ST and type-A cases formed cracks with relatively smooth surfaces, while the type-D case formed a visibly tortuous crack.

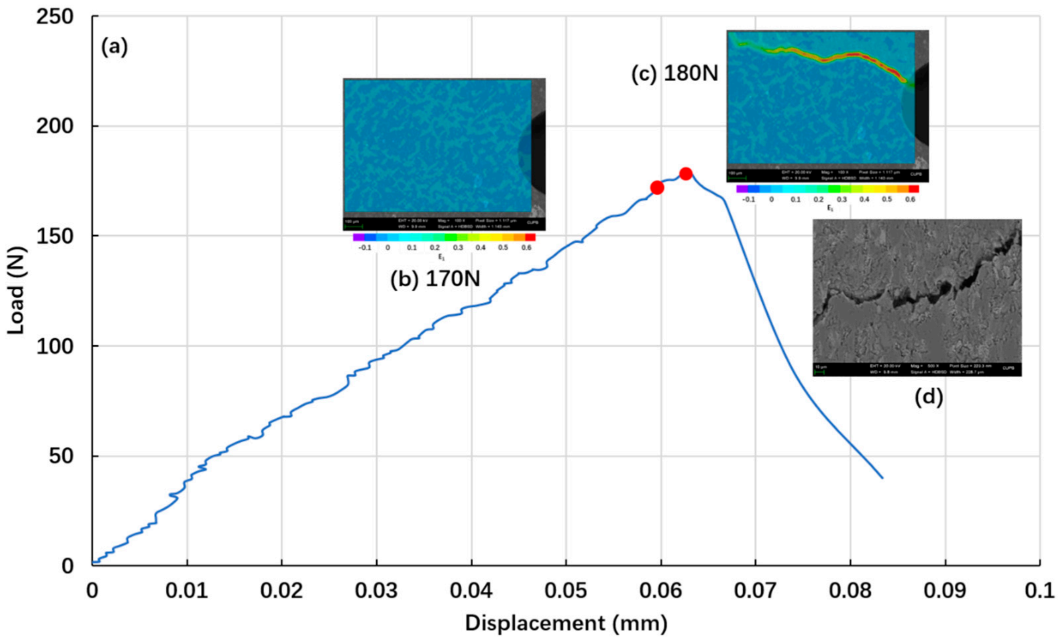

Figure 9. Cracking process in Group D−2: (**a**) load–displacement curve for Group D−2; (**b**) E_1 cloud chart at a load of 170 N; (**c**) E_1 cloud chart at a load of 180 N and (**d**) zoomed out SEM image of the crack.

Figure 10 shows the overall E_1 strain cloud charts of the three-point bending experiments. It can be seen that the crack paths were significantly different for different groups.

For the type-ST crack cases, the loading direction was parallel to the bedding plane, which was a weak plane with a lower structural failure condition. Therefore, the cracks initiated from the prefabricated notch, propagated along the bedding plane and formed a straight main crack that was nearly parallel to the loading direction (Figure 10a–c).

For the type-D crack cases, the crack initiation deviated a certain angle from the loading direction and then continued to turn as they advanced, but their overall trend extended parallel to the loading direction, and the crack paths were connected by multisegment arc-like curves (Figure 10d–f).

For the type-A crack cases, the crack initiation direction and the loading direction were often at an angle of approximately 30° to 45° and extended forward. The crack paths can be a relatively straight main crack or bifurcation and turning cracks (Figure 10g,h). Additionally, the type-A crack length was usually more than double that of the type-ST and type-D cases.

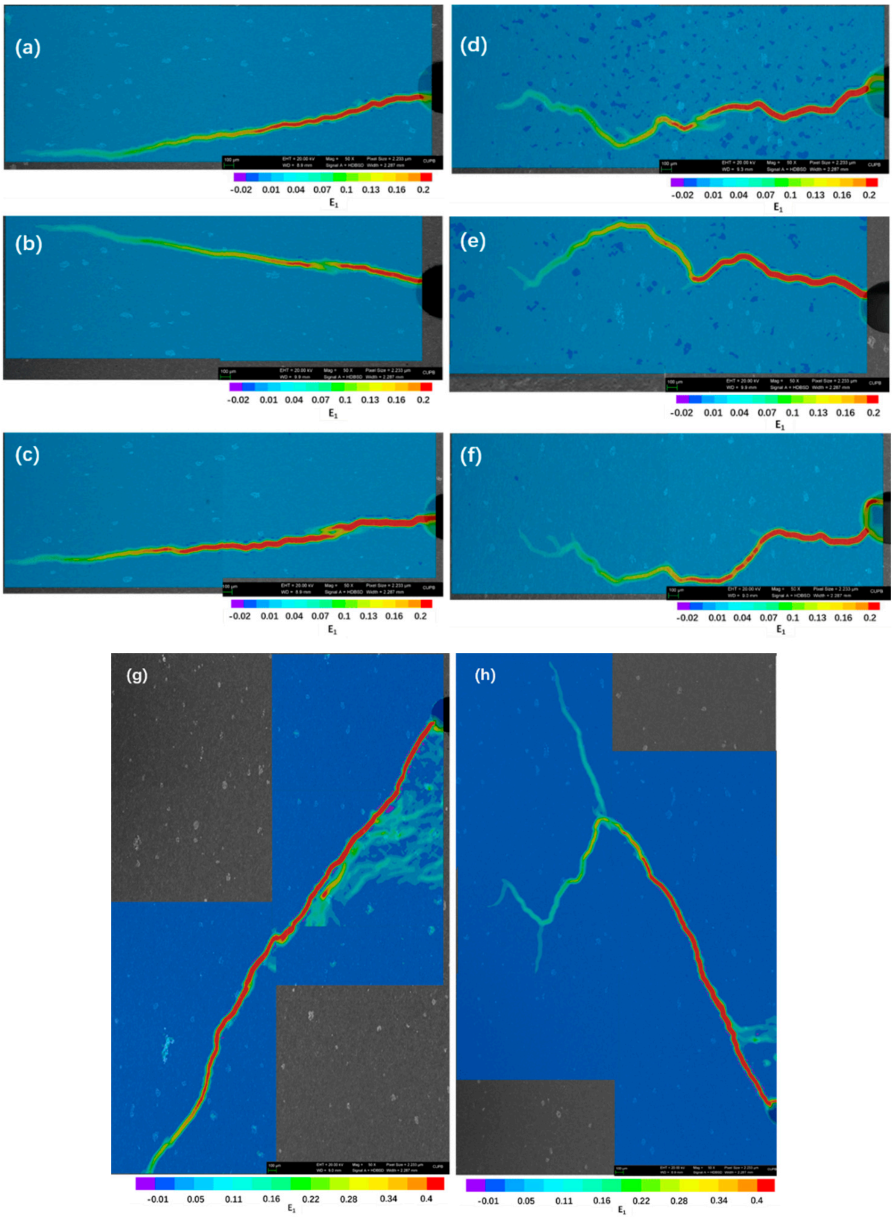

Figure 10. Crack paths in the three-point bending experiment: (**a**–**c**) are type−ST crack cases; (**d**–**f**) are type−D crack cases; and (**g**,**h**) are type−A crack cases.

3.3. Anisotropy of Microscopic Mechanical Properties

To investigate the microscopic anisotropy of the shale specimens, we further calculated several critical mechanical property parameters based on the laboratory testing results. The studied microscopic mechanical properties include the elastic modulus and compressive strength obtained from compression tests and the tensile strength, fracture toughness and elastic-bending modulus obtained from three-point bending tests. By comparing the calculated microscopic mechanical properties of different test groups, the anisotropic feature of shale specimens can be understood.

The elastic moduli for different test groups were calculated based on the axial strain (ε_{xx} results from DIC analysis with Equation (1). The DIC strain values represent the average of the full-field strain values within the region of interest. Figure 11 shows that the elastic moduli presented a U-shaped characteristic of first falling and then rising. The smallest elastic modulus appeared in the case of $\theta = 60°$, and the largest case is $\theta = 0°$.

$$E = \frac{\sigma_x}{\varepsilon_{xx}} \tag{1}$$

where E is the elastic moduli, σ_x is the compressive stress and ε_{xx} is the axial strain.

Moreover, the uniaxial compressive strength of rock refers to the load that the rock specimen can bear per unit area when it is compressed in one direction to failure. Affected by the bedding characteristics, the compressive strength of shale usually exhibits obvious macroscopic anisotropy characteristics. In this study, the uniaxial compressive strength was obtained by recording the peak loads of each specimen during the uniaxial compression experiments shown in Table 2. The experimental results in this study indicated that the microscopic compressive strength also showed similar anisotropic characteristics. The compressive strength was strongly related to the bedding angle θ. Figure 11 shows that the compressive strength was the lowest when $\theta = 30°$ and the highest when $\theta = 90°$; when $\theta = 0°$or 60°, the compressive strengths were similar.

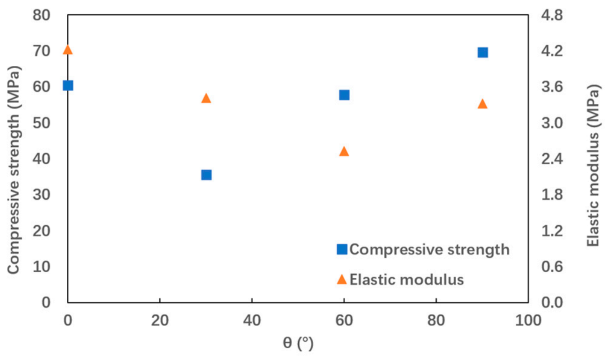

Figure 11. Compressive strength and elastic modulus of shale specimens with different bedding angles.

The anisotropy of the compressive strength and elastic modulus can also be understood by studying the shear strain changes with increasing stress for different bedding angle cases (Figure 12). There was the maximum shear strain when $\theta = 30°$, especially for higher stress conditions, which caused the shale specimen to fail more easily. The situation was reversed when $\theta = 90°$ since we can see that the much smaller shear strain led to the maximum compressive strength.

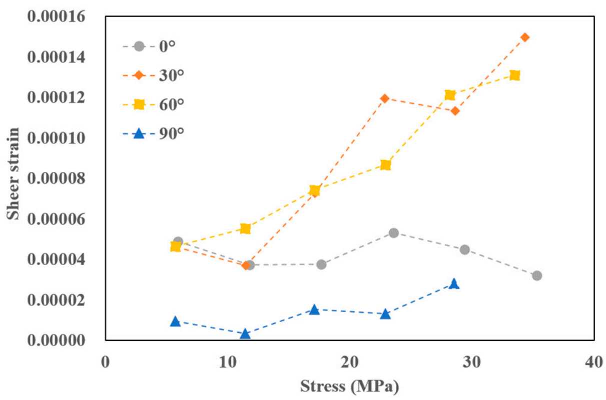

Figure 12. Scatter plot of the stress-shear strain of shale specimens with different bedding angles.

For the shale specimens used in the three-point bending tests, we can assume that the tensile stress and compressive stress are symmetrically distributed along the centerline, and the tensile strength of the sample can be expressed by the following equation:

$$\sigma_t = \frac{3P_{\max}S}{2t(H-a)^2} \tag{2}$$

where σ_t is the tensile strength in MPa, $P_{\max}$ is the peak load of the shale specimen in N, S is the effective bean span in m, a is the length of the preset notch in m and t and H are the thickness and width of the specimen, both in the unit of m, respectively.

In addition, fracture toughness is one of the inherent properties of rock materials, which can characterize the rock's ability to resist crack initiation and propagation. According to the handbook for stress analysis of cracks [28], the mode I fracture toughness K_{IC} for a single-edge notched three-point bending specimen can be determined by

$$K_{IC} = \frac{P_{\max}S}{tH^{1.5}}\left[2.9\left(\frac{a}{H}\right)^{0.5} - 4.6\left(\frac{a}{H}\right)^{1.5} + 21.8\left(\frac{a}{H}\right)^{2.5} - 37.6\left(\frac{a}{H}\right)^{3.5} + 38.7\left(\frac{a}{H}\right)^{4.5}\right] \tag{3}$$

where the parameters have the same physical meanings and units as those in Equation (2).

The elastic-bending modulus characterizes the ability of rock materials to resist flexural deformation within the elastic limit and is an important parameter that can be obtained in three-point bending tests. Based on the slope k of the elastic segment of the load–displacement curves, the elastic-bending modulus can be expressed as [29],

$$E_s = \frac{S^3}{4t(H-a)^3}k \tag{4}$$

where E_s is the elastic-bending modulus in Pa, k is the slope of the elastic segment of the load–displacement curves, S is the effective bean span in m, a is the length of the preset notch in m, and t and H are the thickness and width of the specimen, both in the unit of m, respectively.

The peak load can be obtained directly from the load–displacement curve of the three-point bending tests. Therefore, based on Equations (1)–(3), we can calculate the tensile strength, fracture toughness and elastic-bending modulus of the nine specimens in the three-point bending tests, respectively. We also used the image processing toolbox in MATLAB and measured the total crack length for each test by counting the pixels of the crack path, and all of the above results are shown in Figure 13.

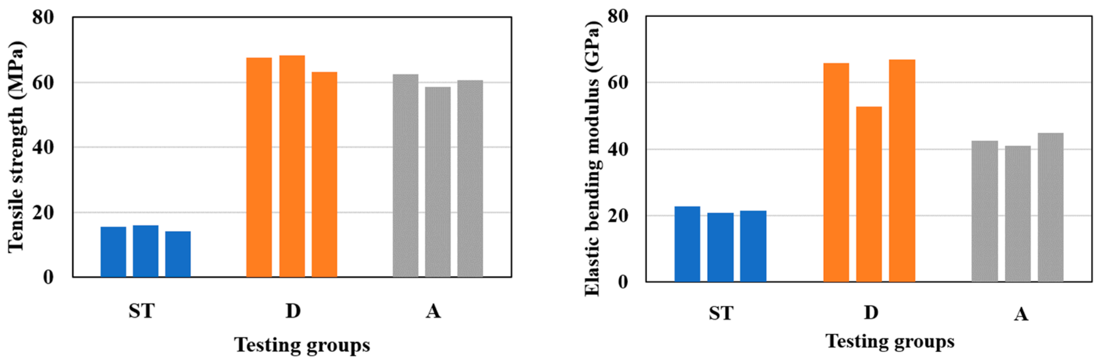

(**a**) (**b**)

Figure 13. *Cont.*

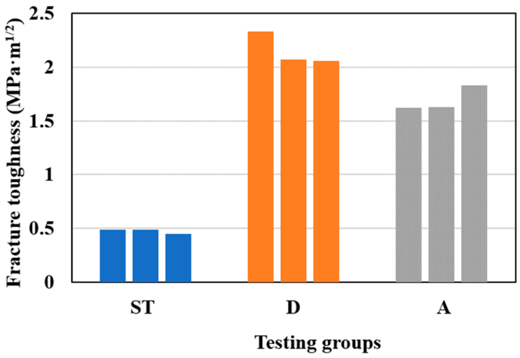

(c)

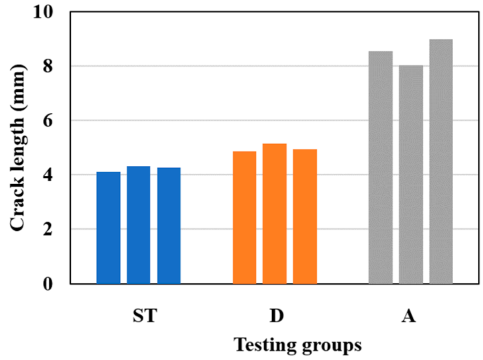

(d)

Figure 13. Fracture property parameters calculated from three-point bending tests: (**a**) tensile strength; (**b**) elastic-bending modulus; (**c**) fracture toughness; and (**d**) crack length.

For the type-ST cases, the cracks were more likely to follow the bedding planes. Since the bedding planes were weak planes, the loads required for the specimen to form the cracks were much lower than those of the other two groups. The lengths of the main cracks were the shortest, and various fracture parameters were also the lowest. This indicates that the specimens of the type-ST groups were more prone to cracking.

For the type-D cases, cracks must simultaneously extend across multiple bedding planes of the shale. Therefore, the peak loads of the specimens were relatively high, and the fracture length was relatively short, but their tensile strengths, fracture toughness and elastic-bending moduli were the highest among the three groups of experiments.

For the type-A cases, the main cracks passed through the bedding planes in sequence. Therefore, the loads required for the specimens to form the cracks were the highest, and the main cracks formed were the longest. Since the main cracks neither developed along the bedding planes nor crossed multiple bedding planes simultaneously, their tensile strengths, fracture toughness and elastic-bending moduli were between those of the type-ST and type-D cases.

4. Conclusions

In this paper, shale outcrop samples from the Changqing area were used to conduct FE-SEM uniaxial compression and three-point bending experiments, and the DIC method was used to analyze the strain field. The micromechanical properties and anisotropic characteristics of the deformation process were studied, and the relevant conclusions were obtained as follows.

(1) During the loading process of the compression experiments, the microscopic deformations of the shale specimens were mainly concentrated in the clay mineral accumulation area and at the microcracks. Most of the microcracks were aligned with the bedding plane direction, and the compression loading led to the expansion or compression of the microcracks for different bedding angle cases. Meanwhile, due to the disordered arrangement of clay minerals, the shear strain was generated and resulted in the simultaneous concentration of positive and negative strains in the clay minerals.

(2) The microscopic anisotropy revealed by the cracking processes and crack paths in the three-point bending tests are strongly related to the crack-bedding orientation relationship. The type-ST and type-A cases both showed clear crack initiation and formed a relatively smooth crack surface, while the type-D cases showed the highest peak loads, more abrupt breaks and formed visibly tortuous cracks, which was consistent with their high fracture toughness and elastic-bending modulus parameters. Additionally, the type-A cases developed the longest cracks among the three testing groups.

(3) For the investigated shale specimens in compression tests, both the peak load and the compressive strength were lower when the bedding angle was 30°, and the elastic

moduli were lower when the bedding angle was 60°. The corresponding shear strain results calculated by the DIC method showed that the shear deformations were larger when the bedding angles were 30° and 60°.

(4) The parameters of the peak load, tensile strength, fracture toughness and elastic-bending modulus of shale specimens also showed obvious anisotropic characteristics in the three-point bending test. For type-ST crack cases, the above parameters were lower than the type-D and type-A cases.

Author Contributions: Conceptualization, W.S.; methodology, W.S. and Y.W.; software, Y.W.; validation, Y.W., J.L.; formal analysis, Y.W. and W.S.; investigation, Y.W.; resources, W.S.; data curation, Y.W. and J.L.; writing—original draft preparation, Y.W. and J.L.; writing—review and editing, W.S.; visualization, Y.W. and W.S.; supervision, W.S.; project administration, W.S.; funding acquisition, W.S. All authors have read and agreed to the published version of the manuscript.

Funding: This research received no external funding.

Data Availability Statement: Data available on request due to privacy restrictions.

Conflicts of Interest: The authors declare no conflict of interest.

References

1. Cao, H.; Gao, Q.; Ye, G.; Zhu, H.; Sun, P. Experimental investigation on anisotropic characteristics of marine shale in Northwestern Hunan, China. *J. Nat. Gas Sci. Eng.* **2020**, *81*, 103421. [CrossRef]
2. Heng, S.; Li, X.; Liu, X.; Chen, Y. Experimental study on the mechanical properties of bedding planes in shale. *J. Nat. Gas Sci. Eng.* **2020**, *76*, 103161. [CrossRef]
3. Niandou, H.; Shao, J.F.; Henry, J.P.; Fourmaintraux, D. Laboratory investigation of the mechanical behaviour of Tournemire shale. *Int. J. Rock Mech. Min. Sci.* **1997**, *34*, 3–16. [CrossRef]
4. Kuila, U.; Dewhurst, D.; Siggins, A.; Raven, M. Stress anisotropy and velocity anisotropy in low porosity shale. *Tectonophysics* **2011**, *503*, 34–44. [CrossRef]
5. Cho, J.W.; Kim, H.; Jeon, S.; Min, K.B. Deformation and strength anisotropy of Asan gneiss, Boryeong shale, and Yeoncheon schist. *Int. J. Rock Mech. Min. Sci.* **2012**, *50*, 158–169. [CrossRef]
6. Lo, T.; Coyner, K.B.; Toksöz, M.N. Experimental determination of elastic anisotropy of Berea sandstone, Chicopee shale, and Chelmsford granite. *Geophysics* **1986**, *51*, 164–171. [CrossRef]
7. Luo, Y.; Xie, H.P.; Ren, L.; Zhang, R.; Li, C.B.; Gao, C. Linear Elastic Fracture Mechanics Characterization of an Anisotropic Shale. *Sci. Rep.* **2018**, *8*, 8505. [CrossRef]
8. Zuo, J.; Lu, J.; Ghandriz, R.; Wang, J.; Li, Y.; Zhang, X.; Li, J.; Li, H. Mesoscale fracture behavior of Longmaxi outcrop shale with different bedding angles: Experimental and numerical investigations. *J. Rock Mech. Geotech. Eng.* **2020**, *12*, 89–101. [CrossRef]
9. Chandler, M.R.; Meredith, P.G.; Brantut, N.; Crawford, B.R. Fracture toughness anisotropy in shale. *J. Geophys. Res. Solid Earth* **2016**, *121*, 1706–1729. [CrossRef]
10. Chong, Z.; Li, X.; Hou, P.; Wu, Y.; Zhang, J.; Chen, T.; Liang, S. Numerical Investigation of Bedding Plane Parameters of Transversely Isotropic Shale. *Rock Mech. Rock Eng.* **2017**, *50*, 1183–1204. [CrossRef]
11. Yoon, J. Application of experimental design and optimization to PFC model calibration in uniaxial compression simulation. *Int. J. Rock Mech. Min. Sci.* **2007**, *44*, 871–889. [CrossRef]
12. Lu, Y.; Li, W.; Wang, L.; Meng, X.; Wang, B.; Zhang, K.; Zhang, X. In-situ microscale visualization experiments on microcracking and microdeformation behaviour around a pre-crack tip in a three-point bending sandstone. *Int. J. Rock Mech. Min. Sci.* **2019**, *114*, 175–185. [CrossRef]
13. Wang, L.; Bornert, M.; Héripré, E.; Chanchole, S.; Pouya, A.; Halphen, B. Microscale insight into the influence of humidity on the mechanical behavior of mudstones. *J. Geophys. Res. Solid Earth* **2015**, *120*, 3173–3186. [CrossRef]
14. Wang, L.L.; Zhang, G.Q.; Hallais, S.; Tanguy, A.; Yang, D.S. Swelling of Shales: A Multiscale Experimental Investigation. *Energy Fuels* **2017**, *31*, 10442–10451. [CrossRef]
15. Zhou, J.; Zeng, Y.; Guo, Y.; Chang, X.; Liu, L.; Wang, L.; Hou, Z.; Yang, C. Effect of natural filling fracture on the cracking process of shale Brazilian disc containing a central straight notched flaw. *J. Pet. Sci. Eng.* **2020**, *196*, 107993. [CrossRef]
16. Li, Y.; Wang, S.; Zheng, L.; Zhao, S.; Zuo, J. Evaluation of the fracture mechanisms and criteria of bedding shale based on three-point bending experiment. *Eng. Fract. Mech.* **2021**, *255*, 107913. [CrossRef]
17. Gao, Q.; Tao, J.; Hu, J.; Yu, X. Laboratory study on the mechanical behaviors of an anisotropic shale rock. *J. Rock Mech. Geotech. Eng.* **2015**, *7*, 213–219. [CrossRef]
18. Bennett, K.C.; Berla, L.A.; Nix, W.D.; Borja, R.I. Instrumented nanoindentation and 3D mechanistic modeling of a shale at multiple scales. *Acta Geotech.* **2015**, *10*, 1–14. [CrossRef]

19. Eliyahu, M.; Emmanuel, S.; Day-Stirrat, R.J.; Macaulay, C.I. Mechanical properties of organic matter in shales mapped at the nanometer scale. *Mar. Pet. Geol.* **2015**, *59*, 294–304. [CrossRef]
20. Wu, Y.; Li, Y.; Luo, S.; Lu, M.; Zhou, N.; Wang, D.; Zhang, G. Multiscale elastic anisotropy of a shale characterized by cross-scale big data nanoindentation. *Int. J. Rock Mech. Min. Sci.* **2020**, *134*, 104458. [CrossRef]
21. Schmidt, R.A. Fracture Mechanics Of Oil Shale-Unconfined Fracture Toughness, Stress Corrosion Cracking, And Tension Test Results. ARMA-77-0082. In Proceedings of the 18th U.S. Symposium on Rock Mechanics (USRMS), Golden, CO, USA, 22–24 June 1977.
22. Chong, K.P.; Kuruppu, M.D.; Kuszmaul, J.S. Fracture toughness determination of layered materials. *Eng. Fract. Mech.* **1987**, *28*, 43–54. [CrossRef]
23. Swan, G.; Cook, J.; Bruce, S.; Meehan, R. Strain rate effects in Kimmeridge bay shale. *Int. J. Rock Mech. Min. Sci. Geomech. Abstr.* **1989**, *26*, 135–149. [CrossRef]
24. Maqsood, Z.; Koseki, J.; Ahsan, K.; Shaikh, M.; Kyokawa, H. Experimental study on hardening characteristics and loading rate dependent mechanical behaviour of gypsum mixed sand. *Constr. Build. Mater.* **2020**, *262*, 119992. [CrossRef]
25. Maqsood, Z.; Koseki, J.; Kyokawa, H. Effects of loading rate on strength and deformation characteristics of gypsum mixed sand. *E3S Web Conf.* **2019**, *92*, 05008. [CrossRef]
26. Maqsood, Z.; Koseki, J.; Miyashita, Y.; Xie, J.; Kyokawa, H. Experimental study on the mechanical behaviour of bounded geomaterials under creep and cyclic loading considering effects of instantaneous strain rates. *Eng. Geol.* **2020**, *276*, 105774. [CrossRef]
27. Loucks, R.G.; Reed, R.M.; Ruppel, S.C.; Hammes, U. Spectrum of pore types and networks in mudrocks and a descriptive classification for matrix-related mudrock pores. *AAPG Bull.* **2012**, *96*, 1071–1098. [CrossRef]
28. Tada, H.; Paris, P.C.; Irwin, G.R. *The Stress Analysis of Cracks Handbook*, 3rd ed.; Tada, H., Ed.; ASME Press: Hoboken, NJ, USA, 2000.
29. Cesar, P.F.; Miranda, W.G.; Braga, R.R. Influence of shade and storage time on the flexural strength, flexural modulus, and hardness of composites used for indirect restorations. *J. Prosthet. Dent.* **2001**, *86*, 289–296. [CrossRef] [PubMed]